CHAPTER III
RESULTS AND DISCUSSION

3.1 Characterizations

3.1.1 Master Curves

The master curves of G' and G'' for high density polyethylene (H5690S and H5603B) at the reference temperature of 160°C are shown in Figures 3.1 and 3.2, respectively. For H5690S, only the terminal zone can be observed while the beginning of entanglement plateau zone can be observed for H5603B.

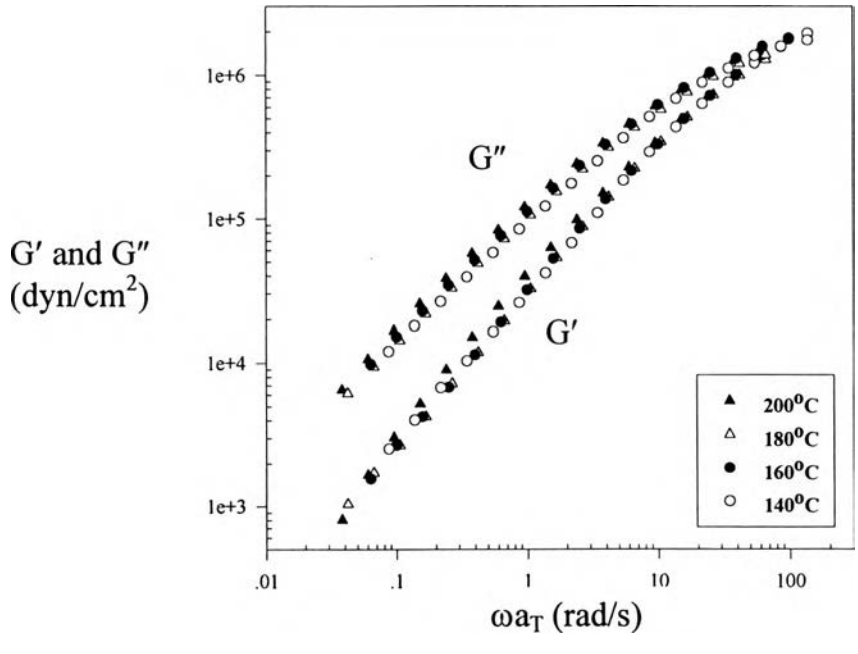

Figure 3.1 Master curves of G' and G'' for H5690S at the reference temperature of 160°C.

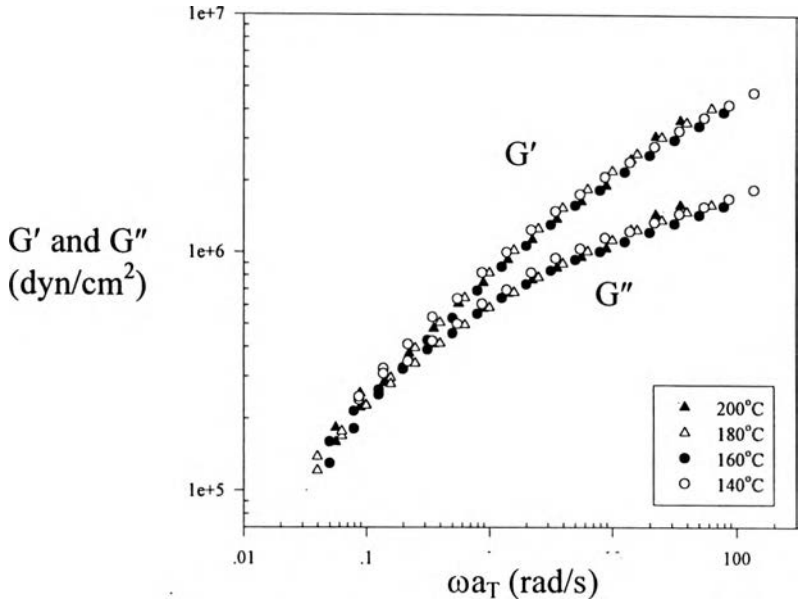

Figure 3.2 Master curves of G' and G'' for H5603B at the reference temperature of 160°C.

The shift factors used in these experiments are tabulated in Table 3.1.

Table 3.1 Horizontal shift factor a_T for each temperature of high density polyethylenes (H5690S and H5603B).

Temperature (°C)	Horizontal Shift Factor (a_T)	
	H5690S	H5603B
200	0.60	0.56
180	0.67	0.79
160	1.00	1.00
140	1.35	1.74

The values of a_T were fitted in Arrhenius equation:

$$ln\ a_T = \frac{E}{R}\left[\frac{1}{T} - \frac{1}{T_o}\right] \qquad ...(15)$$

where E = Activation energy for flow (kJ/mole)

R = Universal gas constant = 8.314 J/mole K

T = Absolute temperature (K)

Experimentally, the activation energy E can be calculated from the slope of the plot of $\ln a_T$ and $[(1/T)-(1/T_o)]$. Then we compared the activation energy from the experiment with the reference value. For H5690S, the slope is equal to 2855.5 and calculated activation energy is equal to 23.7 kJ/mole, close to 27 kJ/mole of the reference (S. H. Wasserman and W. Graessley,1996). For H5603B, the slope is equal to 3240.5 and calculated activation energy is equal to 26.9 kJ/mole, which is also close to the activation energy of the reference.

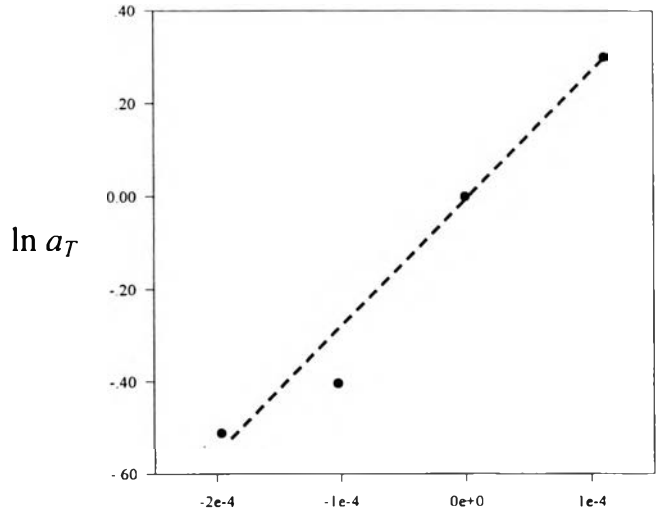

Figure 3.3 Plot of ln a_T and $[(1/T)-(1/T_o)]$ for H5690S.

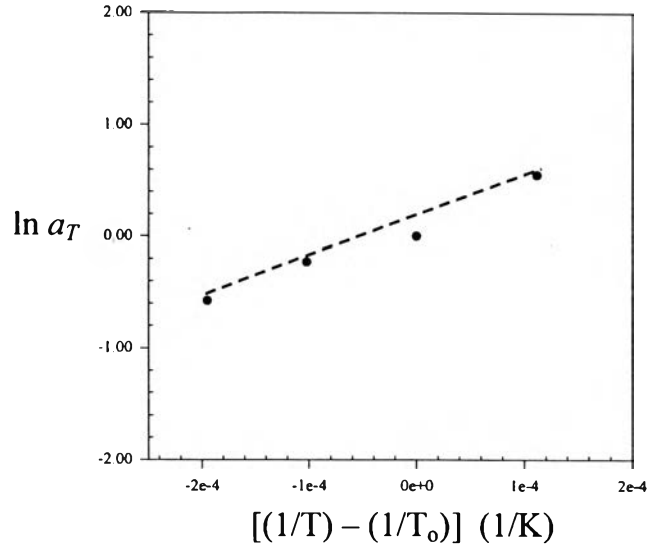

Figure 3.4 Plot of ln a_T and [(1/T) – (1/T$_o$)] for H5603B.

3.1.2 Viscosity

The correlations between viscosity and shear rate for H5690S and H5603B at different temperatures are shown in Figures 3.5 and 3.6, respectively.

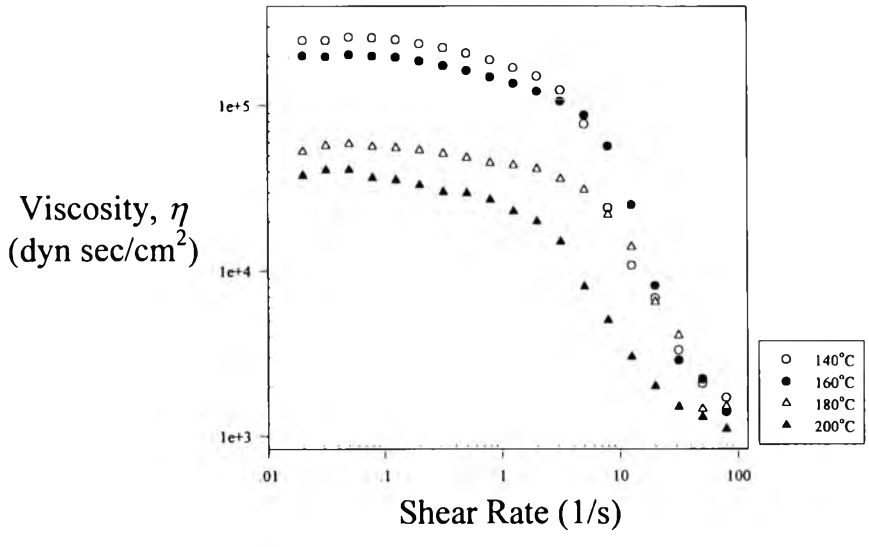

Figure 3.5 Plot of viscosity vs. shear rate for H5690S.

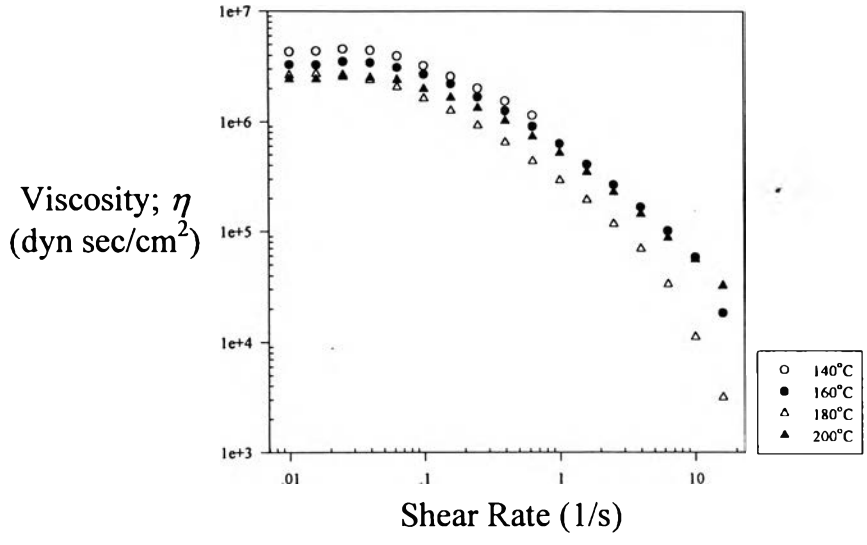

Figure 3.6 Plot of viscosity vs. shear rate for H5603B.

The values of zero shear viscosity η_o at different temperatures for H5690S and H5603B are tabulated in Table 3.2.

Table 3.2 η_o at different temperatures for H5690S and H5603B.

Temp (°C)	η_o (dyn sec/cm^2)	
	H5690S	H5603B
140	2.3×10^5	4.2×10^6
160	2.0×10^5	3.2×10^6
180	5.7×10^4	2.5×10^6
200	4.0×10^4	2.2×10^6

3.1.3 Viscoelastic Regime

Linear and nonlinear viscoelastic regimes of H5690S and H5603B were determined by plotting of complex modulus (G*) vs. strain amplitude. The percentages of strain amplitude dividing linear and nonlinear regimes are tabulated in Table 3.3.

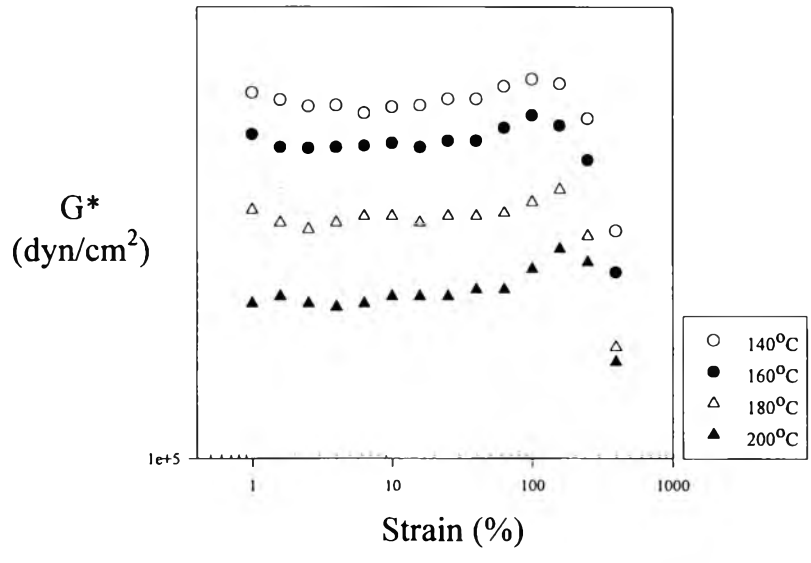

Figure 3.7 Plot of complex modulus *G** vs. strain for H5690S.

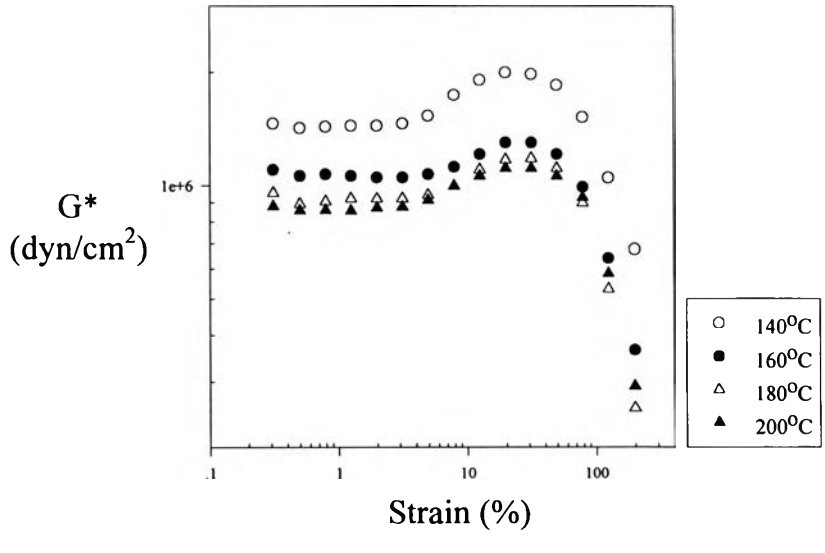

Figure 3.8 Plot of complex modulus *G** vs. strain for H5603B.

Table 3.3 Linear and nonlinear viscoelastic regimes.

Temp (°C)	Strain Amplitude (%)	
	H5690S	H5603B
140	50	4
160	50	4
180	80	4
200	80	4

3.2 Critical Conditions

3.2.1 Critical Conditions for Decay in Complex Modulus

When shear force is imposed on a viscoelastic material, fracture can be formed which leads to a decaying in complex modulus with time. Complex modulus was observed as a function of time in order to monitor the surface interaction between polymer melt and solid surface. The experiments were done in both linear viscoelastic regime (LVR) and nonlinear viscoelastic regime (NVR) at the temperatures of 160, 180, and 200°C. The results from LVR and NVR show the same trend; when the applied frequency reaches the critical values, G^* will decay. The critical frequency for G^* decay (ω_d^*) is defined as "the minimum frequency that G^* starts to decays more than a factor of 2 within 2 hours" (Chen et al., 1994). Plot of complex modulus G^* vs. time for H5690S sheared at the amplitude of 30% at 160°C is shown in Figure 3.9.

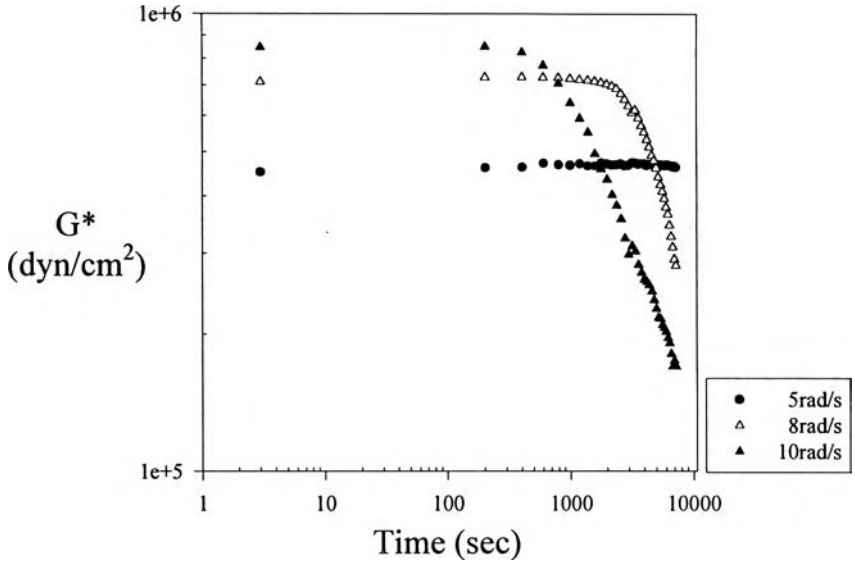

Figure 3.9 Plot between complex modulus G^* vs. time for H5690S sheared at an amplitude of 30% at 160°C.

At 5 rad/s, G^* did not change with time but when the frequency was increased to 8 rad/s G^* decayed more than a factor of 2 within 2 hours while above this frequency G^* sharply decayed with time. In this case, G^* decays at ω_d^* of 8 rad/s. Plot of G^* vs. time for H5690S sheared at an amplitude of 30% at 180°C is shown in Figure 3.10; ω_d^* is equal to 10 rad/s.

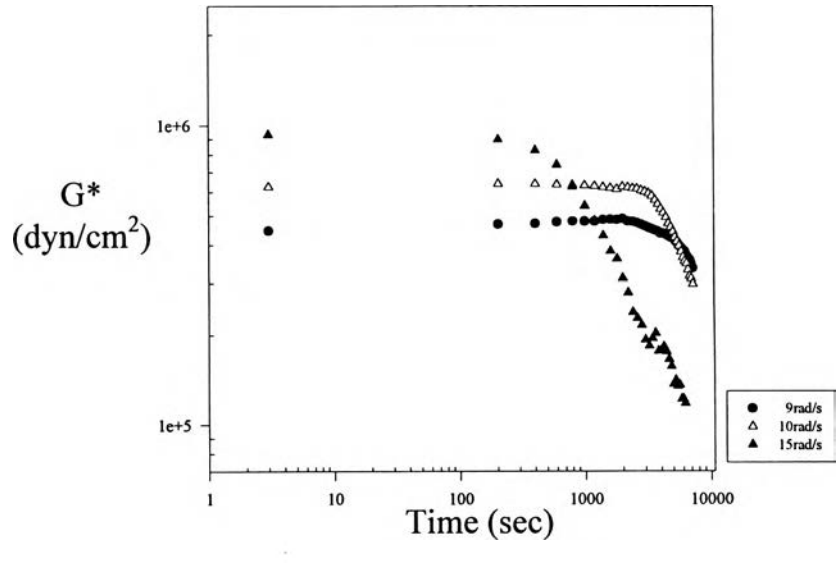

Figure 3.10 Plot between complex modulus G^* vs. time for H5690S sheared at an amplitude of 30% at 180°C.

Different result was observed at 200°C; G^* rose at low frequency but decayed at high frequency. In this case, critical frequency for rising in G^* (ω_r^*) has been defined as "the maximum frequency that G^* starts to rises more than a factor of 2 within 2 hours". For 200°C in LVR, G^* rises at ω_r^* and decays at ω_d^* equal to 10 and 20 rad/s, respectively.

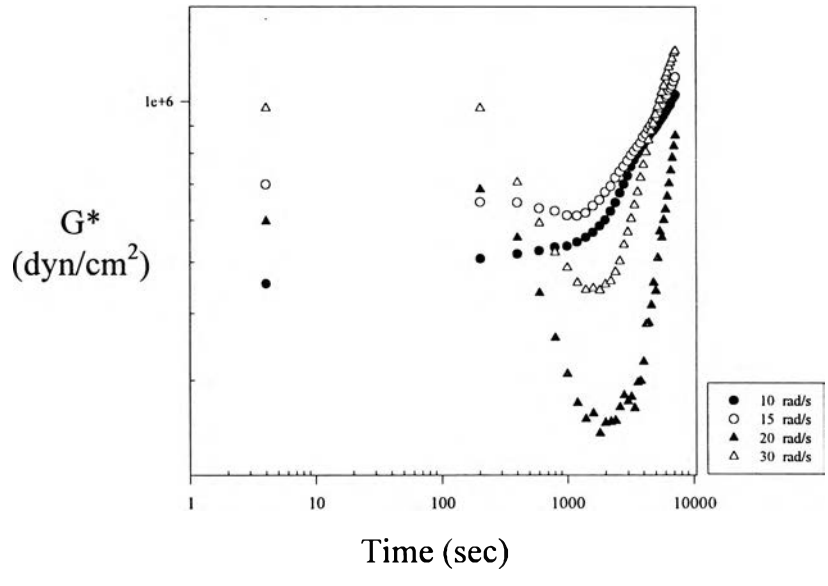

Fig 3.11 Plot of complex modulus G^* vs. time for H5690S sheared at an amplitude of 30% at 200°C.

Tables 3.4 and 3.5 show the critical frequencies and critical stresses at different strain amplitudes and temperatures, respectively.

Table 3.4 Critical frequency at different strain amplitudes at the temperatures of 160, 180, and 200°C for H5690S.

% Strain	Critical Frequency ω_d* (rad/s)		
	160°C	180 °C	200 °C
15	41.0	43.0	-
20	-	-	45.0
30	8.0	8.6	20.0
50	5.0	3.5	11.0
70	2.0	2.1±0.07	5.0
150	0.6	0.7	2.0
300	0.3±0.00	0.4	0.55±0.07

Table 3.5 Critical stress at different strain amplitudes at the temperatures of 160, 180, and 200°C for H5690S.

% Strain	Critical Stress (dyn/cm^2)		
	160°C	180 °C	200 °C
15	2.40 x 10^5	1.90 x 10^5	-
20	-	-	3.50 x 10^5
30	2.16 x 10^5	1.62 x 10^5	3.00 x 10^5
50	1.80 x 10^5	1.38 x 10^5	2.70 x 10^5
70	1.49 x 10^5	1.26±0.04 x 10^5	2.00 x 10^5
150	1.42 x 10^5	1.19 x 10^5	1.80 x 10^5
300	1.38±0.02 x 10^5	1.15 x 10^5	1.67±0.04 x 10^5

3.2.2 Effect of Temperature

The overall results for the critical conditions are shown in Figures 3.12 (a) and (b), which are the plots of the critical frequency vs. strain imposed and critical frequency vs. the stress imposed, respectively. Critical frequency decreases with increasing strain while it increases with increasing stress.

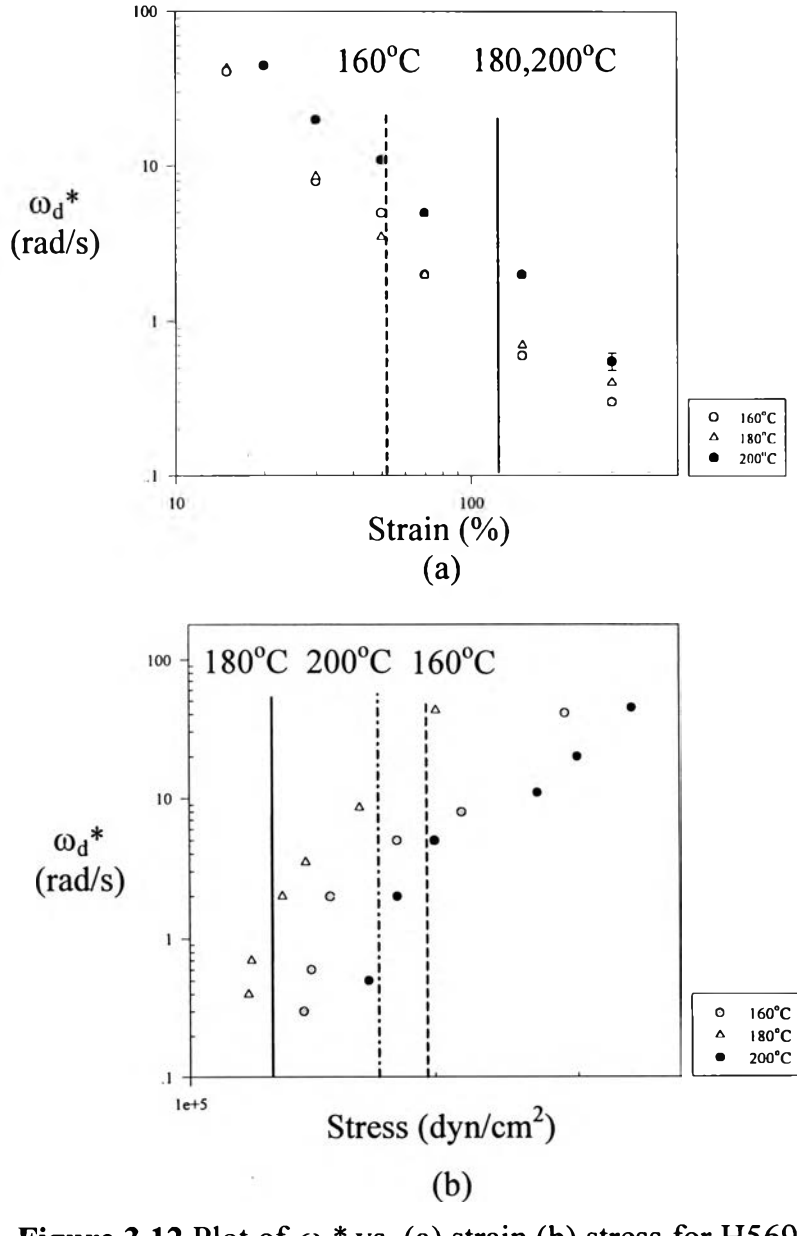

Figure 3.12 Plot of ω_d* vs. (a) strain (b) stress for H5690S at different temperatures.

Figure 3.12 (a) illustrates that critical frequencies at the temperatures of 160 and 180°C are close to each other while at 200°C it is higher than the others.

To find out whether the mechanism of slip for all temperatures is related with the Rouse or Reptation theories, a plot of $\omega_d * \eta_o(T)/T$ vs. stress for H5690S at the temperatures of 160, 180, and 200°C was made. If the data from all temperatures are collapsed with each other, the mechanism of slip for all temperatures can be related with one of these two theories. From the plot of $\omega_d * \eta_o(T)/T$ for H5690S at all temperatures, only the data at 160 and 180°C in NVR are collapsed with each other while they are partially collapsed in LVR. The data at 200°C, the anomalous data, is separated to Part 3.6.

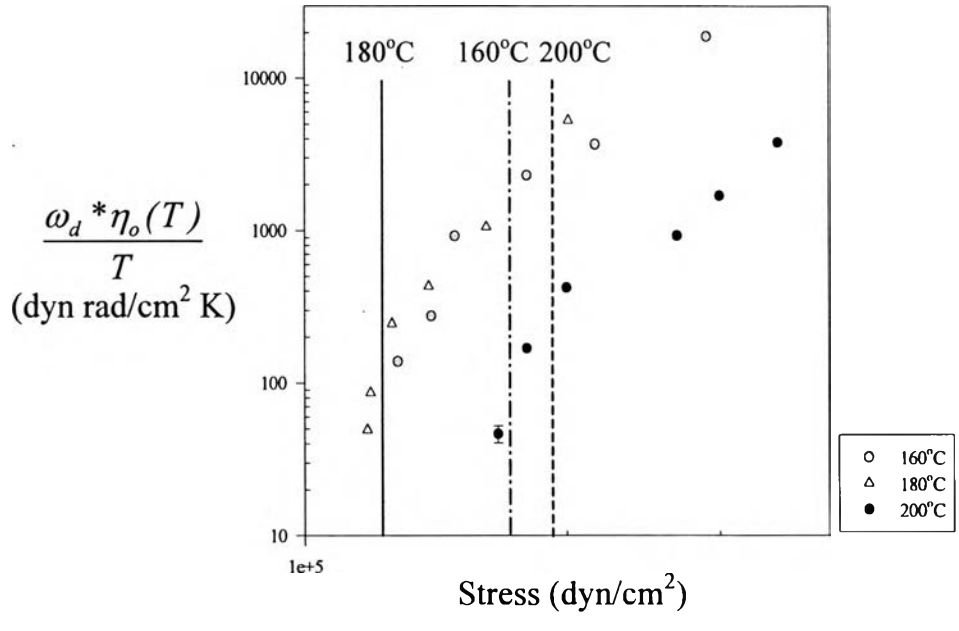

Figure 3.13 Plot of $\omega_d * \eta_o(T) / T$ and stress for H5690S.

3.2.3 Effect of Molecular Weight

Two grades of high density polyethylene (H5690S and H5603B) were used in order to find out whether modified Rouse or Reptation theory is the slip mechanism. The correlation between $\omega_d * \eta_o(T)M$ and $\omega_d * \eta_o(T)M^3$ vs. stress of H5690S and H5603B at the same temperature were investigated. Plots of $\omega_d * \eta_o(T)M$ and $\omega_d * \eta_o(T)M^3$ vs. stress of H5690S and H5603B at 180°C are shown in Figures 3.14 and 3.15, respectively.

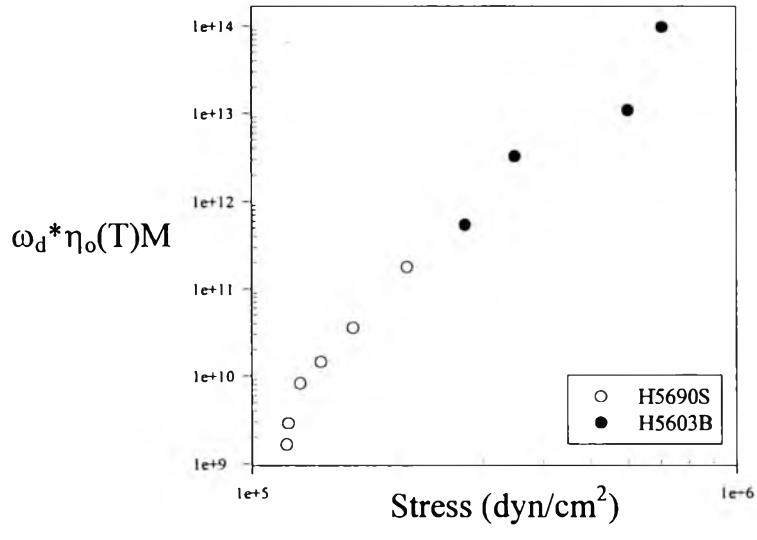

Figure 3.14 Plot of $\omega_d * \eta_o(T)M$ vs. stress for H5690S and H5603B at 180°C.

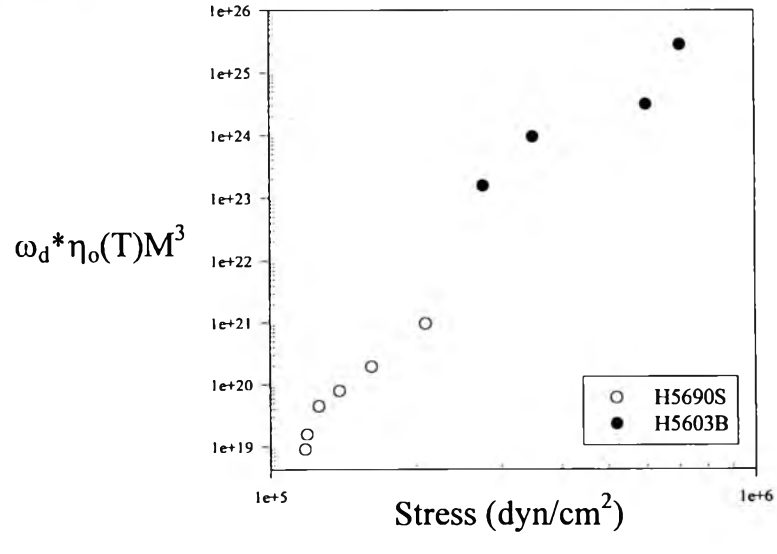

Figure 3.15 Plot of $\omega_d * \eta_o(T)M^3$ vs. stress for H5690S and H5603B at 180°C.

From the plot between $\omega_d * \eta_o(T)M$ vs. stress, the curve of H5690S collapses well with H5603B while they are not collapsed with each other in the plot of $\omega_d * \eta_o(T)M^3$ vs. stress. We deduce that the "Modified Rouse Theory" is related with the slip mechanism. The slip mechanism is possibly desorption between adsorbed polymer chains and solid wall, and certainly not disentanglement.

Plot of $\omega_d * \eta_o(T)M/T$ vs. stress for H5690S at 160 and 180°C and H5603B at 180°C is illustrated in Figure 3.16. All three curves are collapsed with each other further confirms our conclusion above.

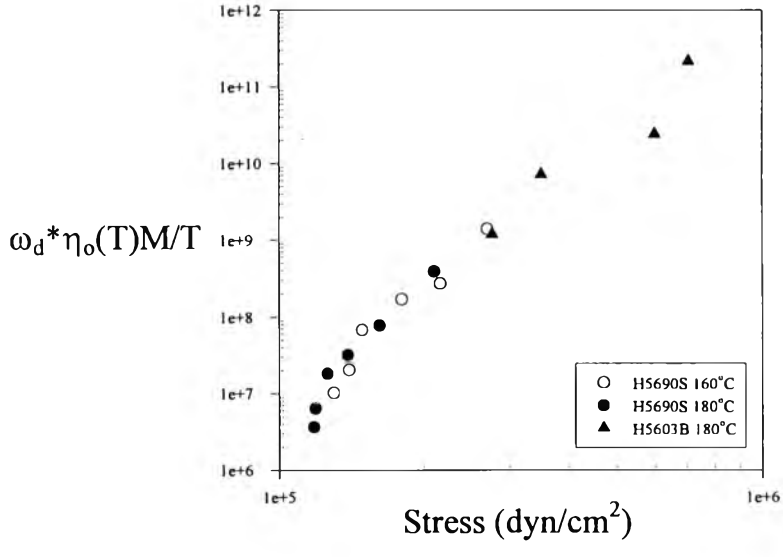

Figure 3.16 Plot of $\omega_d * \eta_o(T)M/T$ vs. stress for H5690S and H5603B at 160 and 180°C.

3.3 Asymptotic Transient Angular Slip

3.3.1 Derivation of Transient Angular Slip

For cone and plate rheometer, the amount of slip can be determined in term of "Transient Angular Slip, $\Delta\theta$", which can be calculated from equations below. The strain and strain rate of cone and plate rheometer can be calculated from equations (16) and (17), respectively,

$$\gamma = \frac{\theta}{\beta} \qquad \ldots(16)$$

$$\dot{\gamma} = \frac{\dot{\theta}}{\beta}$$

or $$f\gamma = \frac{f\theta}{\beta} = \frac{\omega}{\beta} \qquad \ldots(17)$$

where θ = angular displacement (rad), β = cone angle (rad), f = oscillating frequency (1/s), and ω = angular frequency (rad/s).

So, the change in strain rate can be calculated as:

$$\Delta\dot{\gamma} = \frac{\Delta\dot{\theta}}{\beta} = f\frac{\Delta\theta}{\beta} \qquad \ldots(18)$$

But $$f = \frac{\omega}{\gamma\beta} \qquad \ldots(19)$$

so, by substitution equation (19) in (18), change in strain rate is

$$\Delta\dot{\gamma} = \frac{\Delta\theta}{\beta}\frac{\omega}{\beta\gamma}. \qquad \ldots(20)$$

Decay in complex modulus G^* can be calculated from the difference between complex modulus at the beginning of the test $G^*(0)$ and complex modulus at any time $G^*(t)$.

$$\Delta G^*(t) = G^*(0) - G^*(t) \qquad \ldots(21)$$
$$= \eta'(\omega)\,\Delta\dot{\gamma}$$

Transient angular slip can be calculated by substitution Eq. (20) into Eq. (21);

$$\Delta G^*(t) = \eta'(\omega)\,\Delta\theta\,\frac{\omega}{\beta^2\gamma}$$

$$\Delta\theta(t) = \frac{\Delta G^*(t)}{\eta'(\omega)}\,\frac{\beta^2\gamma}{\omega} \qquad \ldots(22)$$

Transient angular slip as a function of time is shown in Figure 3.17.

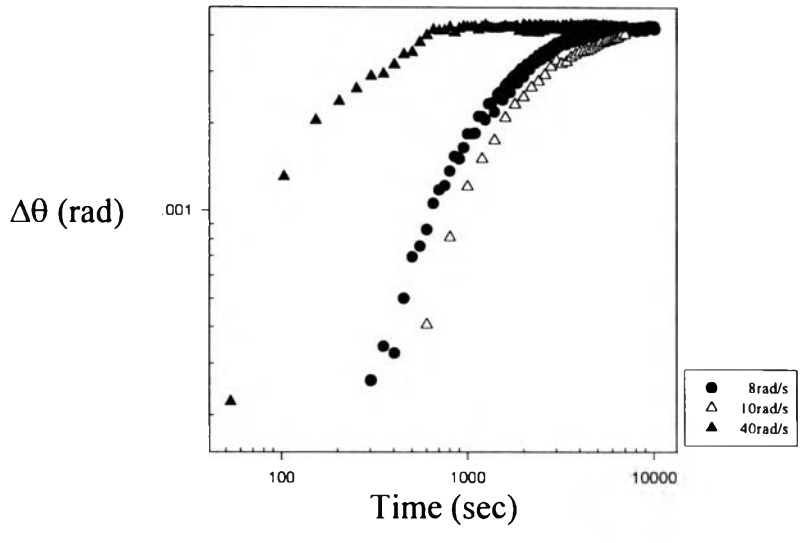

Figure 3.17 Plot of transient angular slip vs. time for H5690S sheared at an amplitude of 30% at 160°C.

Transient angular slip at each frequency reaches the asymptotic value after a sufficiently long period of time, which has been called "asymptotic transient angular slip; $\Delta\theta_{asymptotic}$".

3.3.2 Effect of Strain Rate

Asymptotic transient angular slip was studied as a function of strain rate at 160 and 180°C in both LVR and NVR. The plots of $\Delta\theta_{asymptotic}$ vs. strain rate for H5690S at 160 and 180°C were shown in Figures 3.18 (a) and (b), respectively.

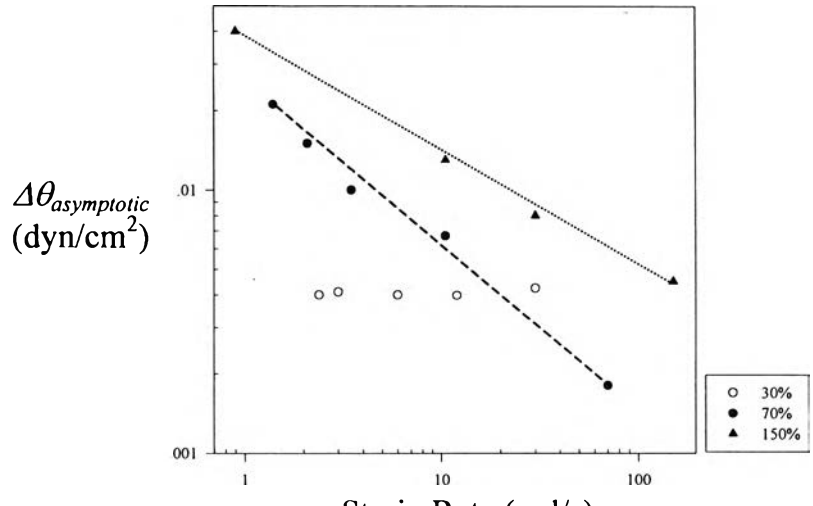

Figure 3.18 Plot of $\Delta\theta_{asymptotic}$ vs. strain rate for H5690S at (a) 160°C and (b) 180°C.

In LVR, $\Delta\theta_{asymptotic}$ is independent of strain rate because the strain is low enough so the rate of desorption is equal to adsorption between adsorbed chains and the wall. But in NVR, $\Delta\theta_{asymptotic}$ critically depends on strain rate at both temperatures because the rate of desorption is too high for the polymer chains to have time to relax.

3.3.3 Effect of Molecular Weight and Temperature

In Part 3.2 we have investigated the slip mechanism at critical condition. In order to determine the slip mechanism after a long period of time after slip occurs, the asymptotic complex modulus $G^*_{asymptotic}$ and the difference between complex modulus at the beginning of the test and complex modulus at the asymptotic point was investigated (ΔG^*).

From modified Rouse theory, when density of the melt is assumed to be the same at the temperatures of 160 and 180°C, the following relations are applicable:

$$G^* \propto \frac{\rho T}{M} \propto \frac{T}{M} \qquad \ldots(23)$$

$$\lambda \propto \frac{M^2}{T} \propto \frac{1}{\dot{\gamma}} . \qquad \ldots(24)$$

From reptation theory, the corresponding relations are:

$$G^* \propto \frac{\eta_o}{\lambda} \propto \frac{\eta_o}{\eta_o} \rho T \qquad \ldots(25)$$

when density is fixed to be the same at the temperatures of 160 and 180°C, so:

$$G^* \propto T \qquad \ldots(26)$$

$$\lambda \propto \frac{\eta_o}{\rho T} \propto \frac{\eta_o}{T} . \qquad \ldots(27)$$

The plots of $\Delta G^*M/T$ and $G^*_{asymptotic}M/T$ vs. $\gamma M^2/T$ for the high density polyethylenes H5690S and H5603B at the temperatures of 160 and 180°C were investigated in order to find out whether desorption is the slip mechanism at long period of time or not.

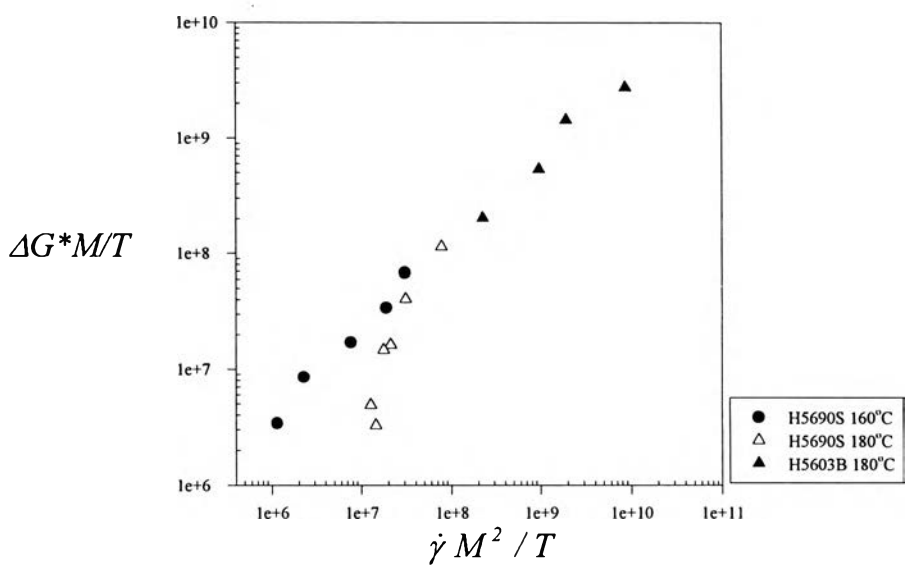

Figure 3.19 Plot of $\Delta G^*M/T$ vs. $\dot{\gamma} M^2/T$ for H5690S and H5603B at 160 and 180°C.

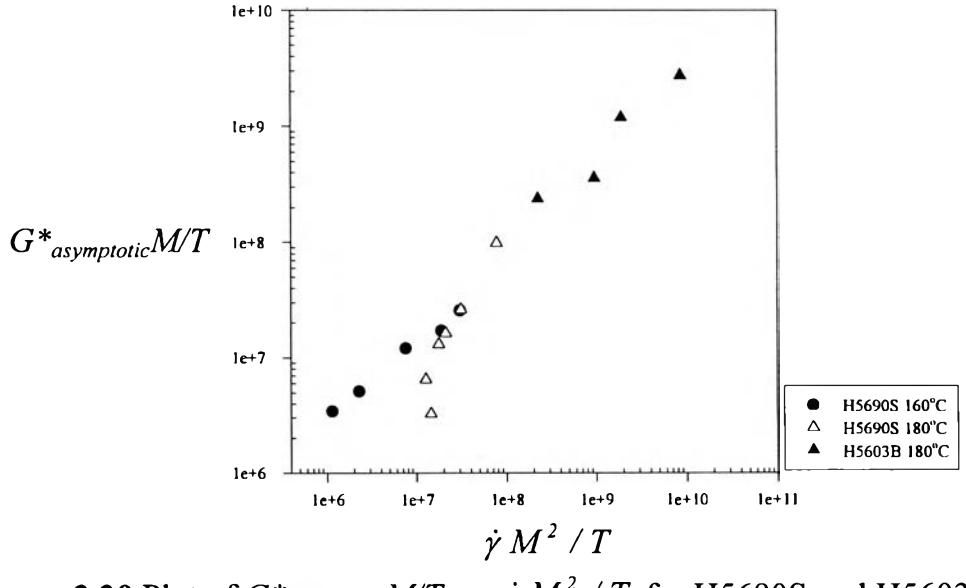

Figure 3.20 Plot of $G^*_{asymptotic}M/T$ vs. $\dot{\gamma} M^2/T$ for H5690S and H5603B at 160 and 180°C.

The plots of $\Delta G^*/T$ and $G^*_{asymptotic}/T$ vs. $\dot{\gamma}\eta_o / T$ for the high density polyethylenes H5690S and H5603B at the temperatures of 160 and 180°C were also investigated in order to prove that disentanglement is the slip mechanism at long period of time or not.

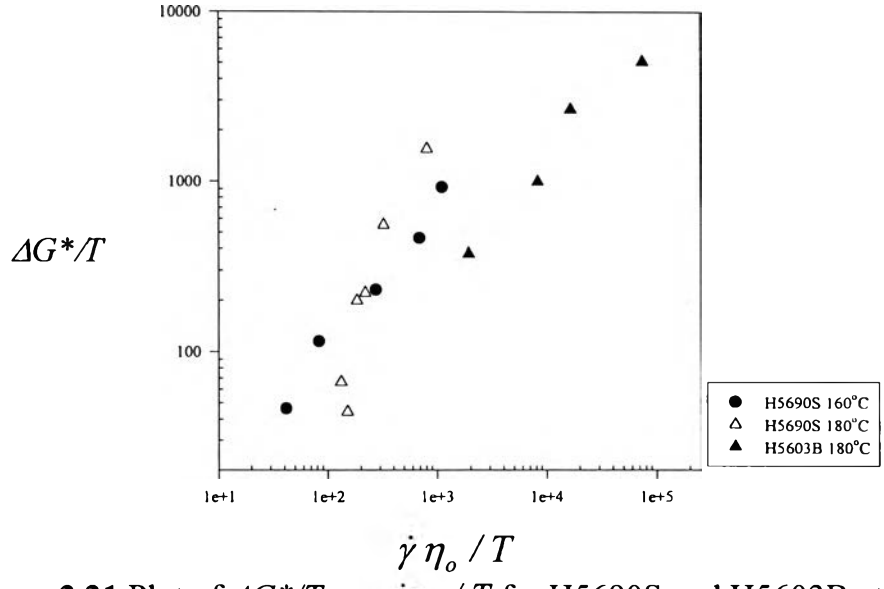

Figure 3.21 Plot of $\Delta G^*/T$ vs. $\dot{\gamma}\eta_o / T$ for H5690S and H5603B at 160 and 180°C.

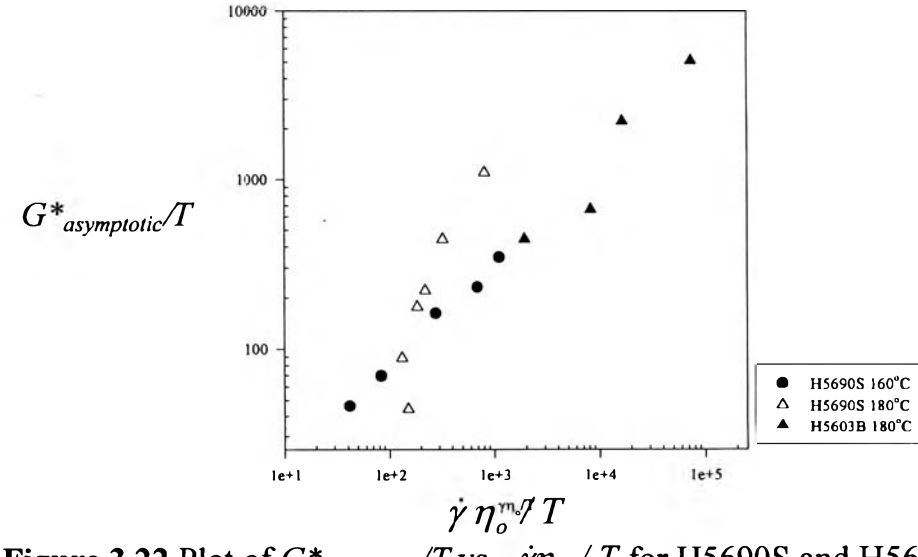

Figure 3.22 Plot of $G^*_{asymptotic}/T$ vs. $\dot{\gamma}\eta_o / T$ for H5690S and H5603B at 160 and 180°C.

ΔG^* and $G^*_{asymptotic}$ show the same trend, so both of them can be used to investigated the slip mechanism at long period after slippage occurs.

Figures 3.19 and 3.20 show good collapse between three data only at high strain rate, while at low strain rate all data are deviated from the others. This means at long period of time after slippage occurs at large strain rate is due to desorption but at low strain rate the slip mechanism is not totally due to desorption.

There is no collapse for all data in Figures 3.21 and 3.22, which implies that disentanglement is not the slip mechanism at long period of time after slippage occurs.

3.4 Slip Velocity and Slip Length

Slip velocity V_s can be derived from equation (22) of transient angular slip $\Delta\theta$.

$$\Delta\vartheta(t) = \frac{\Delta G^*(t)}{\eta'(\omega)} \frac{\beta^2 \gamma}{\omega}$$

$$\Delta\dot{\theta} = \dot{\theta} - \dot{\theta}_m = \Delta\theta f \quad \ldots(28)$$

$$V = \dot{\theta} R \quad \ldots(29)$$

$$V_s = \Delta\dot{\theta} R \quad \ldots(30)$$

where V is the velocity of the solid plate, $\dot{\theta}$ is instrument local angular velocity, $\dot{\theta}_m$ is material local angular velocity, and R is the radius of the solid plate. By substitution equation (28) into (30), slip velocity can be calculated as:

$$V_s = \Delta\theta f R = \Delta\theta \frac{\omega}{2\pi} R \quad \ldots(31)$$

Slip length, the amount of slip, can be derived from slip velocity as:

$$b \equiv \frac{V_s}{\dot{\gamma} - \dot{\gamma}_s} \equiv \frac{\Delta\theta f R}{\frac{\dot{\theta}}{\beta} - \frac{\Delta\dot{\theta}}{\beta}} \quad \ldots(32)$$

where $\dot{\gamma}$ is strain rate and $\dot{\gamma}_s$ is strain rate for slip.

Plots of slip length vs. slip velocity for H5690S at the strain amplitudes of 30% and 150% at 160 and 180°C are shown in Figures 3.23 (a) and (b), respectively. The results of both temperatures show the same trend. In LVR, b is independent of V_s. But in NVR, b sharply decreases with V_s.

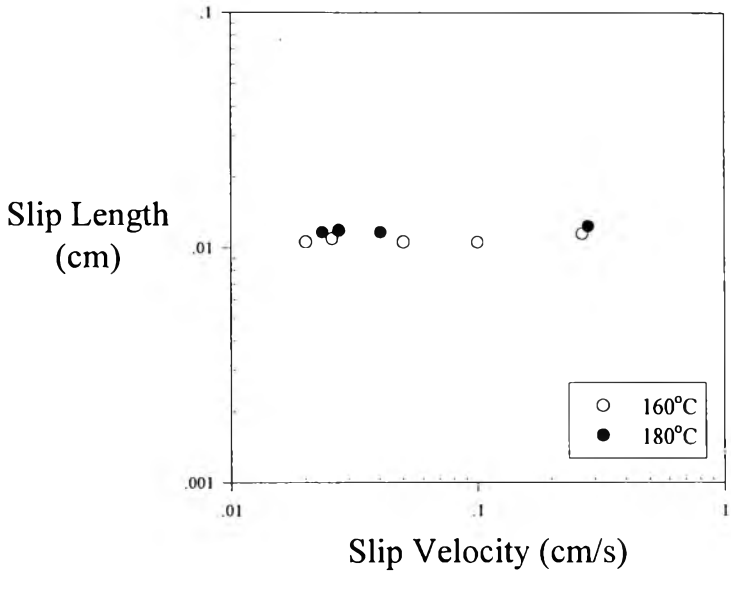

(a)

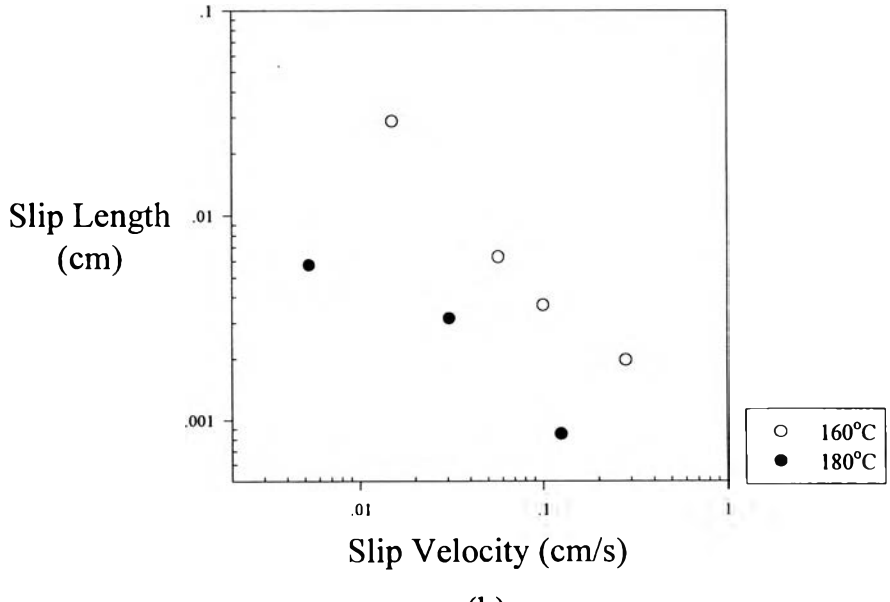

(b)

Figure 3.23 Plot of slip length vs. slip velocity for H5690S at (a) 30% strain and (b) 150% strain at 160°C and 180°C.

Drda and Wang (1995) found that the slip velocity increases with V_s and temperature but the extrapolation length b is independent of temperature. Our results in LVR agree with their finding. But in NVR, b decreases with increasing V_s; this behavior has not been observed before.

Table 3.6 shows the slip velocity and slip length of H5690S at 160 and 180°C in LVR (30% stain) and NVR (150% strain).

Table 3.6 Slip velocity and slip length in LVR and NVR for H5690S.

30% Strain				150% Strain			
160°C		180°C		160°C		180°C	
V_s	b	V_s	b	V_s	b	V_s	b
0.020	0.0106	0.024	0.0116	0.015	0.0288	0.005	0.0057
0.026	0.0109	0.027	0.0119	0.057	0.0063	0.125	0.0008
0.100	0.0105	0.040	0.0116	0.283	0.0020	0.031	0.0032
0.267	0.0114	0.283	0.0123	0.100	0.0036	-	-
0.050	0.0106	-	-	-	-	-	-

3.5 Morphology of Polymers at Interface

The morphologies of the samples were studied by using scanning electron microscope (SEM).

3.5.1 Outer Surfaces

Outer surface textures can be divided into 3 cases:

3.5.1.1 Below Critical Conditions

The high density polyethylene samples (H5690S), after having been sheared below critical conditions (ω_d*) in both LVR and NVR at 160°C, were studied microscopically (magnification = 2,000). The surface textures of the sheared samples in both LVR and NVR have no voids.

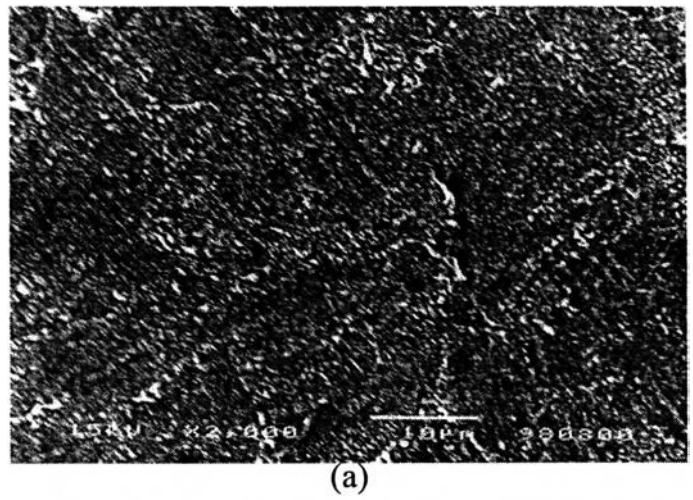

(a)

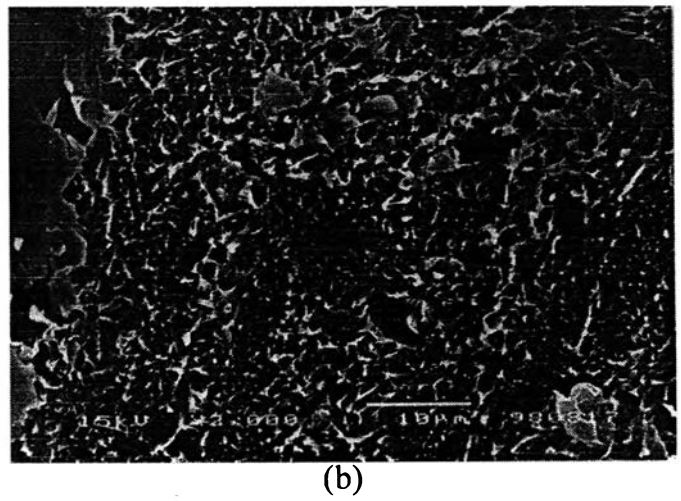

(b)

Figure 3.24 SEM micrographs of the H5690S samples after having been sheared below critical conditions at 160°C in (a) LVR and (b) NVR.

3.5.1.2 Critical Conditions

The H5690S samples, after having been sheared at critical conditions in both LVR and NVR at 160°C, were studied microscopically (magnification = 2,000). Voids occurred on the surfaces in both LVR and NVR.

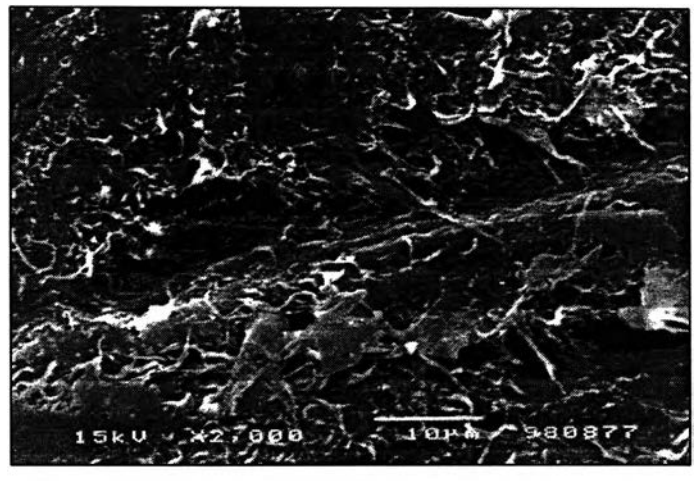

(a)

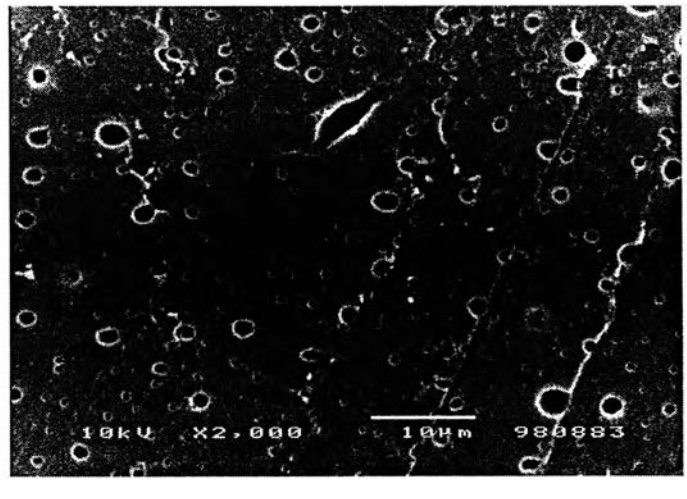

(b)

Figure 3.25 SEM micrographs of the H5690S samples after having been sheared at critical conditions at 160°C in (a) LVR and (b) NVR.

3.5.1.3 Above Critical Conditions

The samples, after having been sheared above critical conditions in both LVR and NVR at 160°C, were studied microscopically (magnification = 2,000). Voids remained only on the surfaces of the sheared samples in LVR while they disappeared in NVR where dimples appeared and require further study. This means that the void formation is one of the cause responsible for the decay in LVR.

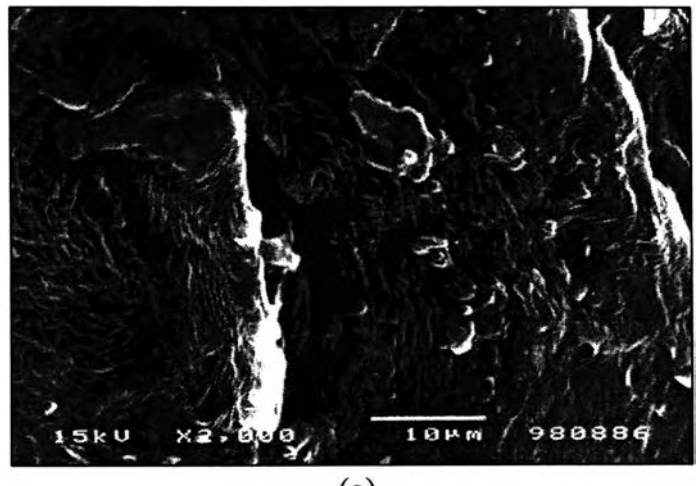

(a)

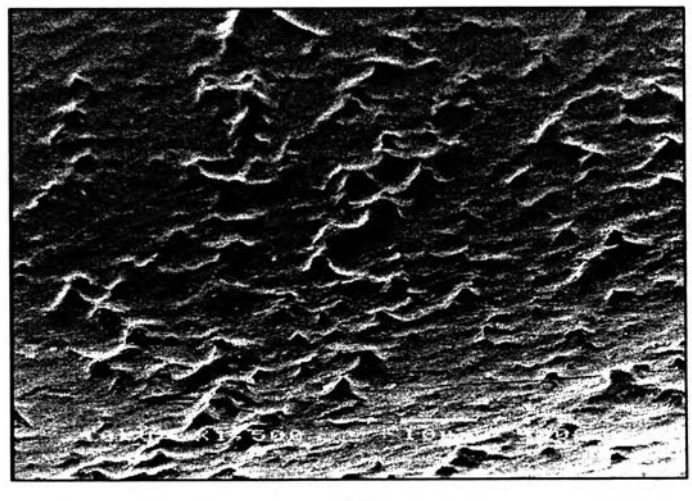

(b)

Figure 3.26 SEM micrographs of the H5690S samples after having been sheared above critical conditions at 160°C in (a) LVR and (b) NVR.

3.5.2 Inner Surfaces

Inner surface is the surface of sheared sample after having been cracked in liquid nitrogen in order to test the mechanism of constitutive instability. If voids occur at both outer and inner surfaces, constitutive instability may be the cause that is responsible for the decay in G^*. Inner surfaces can be divided into 3 cases:

3.5.2.1 Below Critical Conditions

Figures 3.27 (a) and (b) show the SEM micrographs (magnification = 2,000) of H5690S samples after have been sheared in both LVR and NVR at 160°C. No voids occurred in both cases.

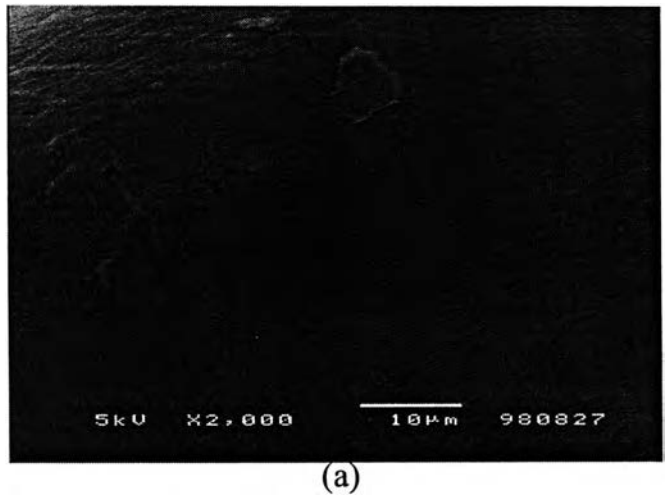

(a)

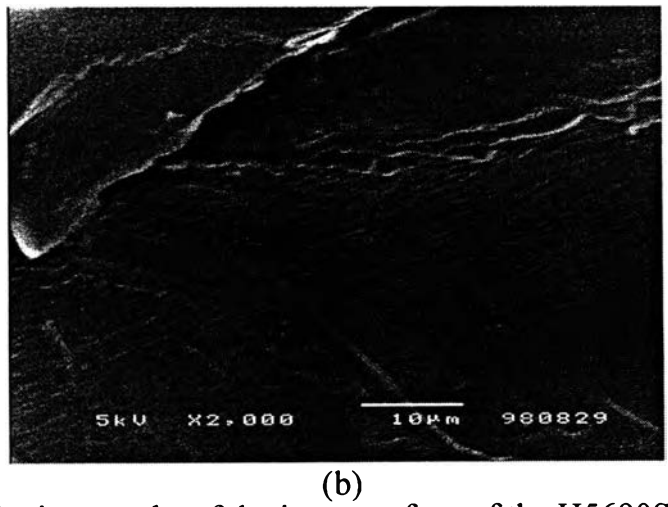

(b)

Figure 3.27 SEM micrographs of the inner surface of the H5690S samples after having been sheared below critical conditions at 160°C in (a) LVR and (b) NVR.

3.5.2.2 Critical Conditions

The sheared H5690S samples were examined by using SEM in both LVR and NVR (magnification = 2,000). No voids occurred in both cases. This means constitutive instability is not the mechanism that make G^* decay.

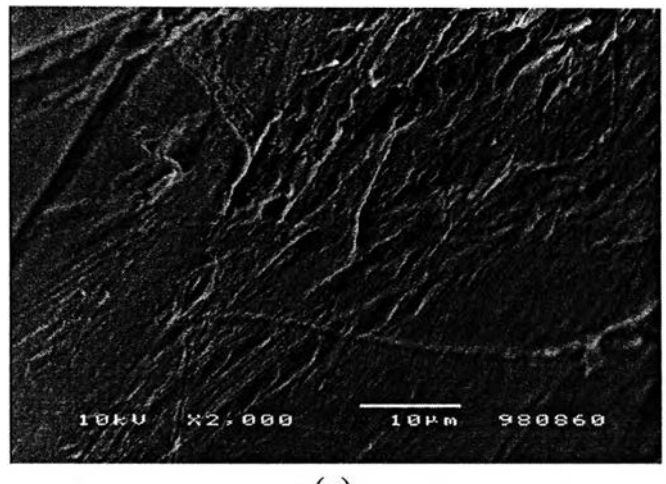

(a)

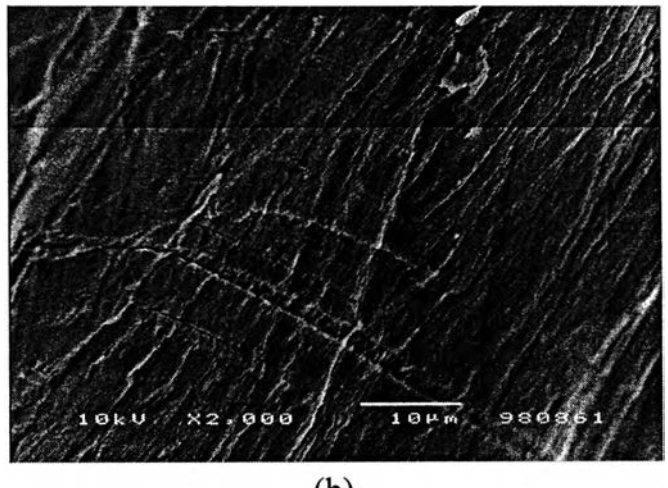

(b)

Figure 3.28 SEM micrographs of the inner surface of the H5690S samples after having been sheared at critical conditions at 160°C in (a) LVR and (b) NVR.

3.6 The Analysis of the Anomalous Data at 200°C

There are 2 critical frequencies; ω_d* and ω_r* so there are also 2 critical stresses; σ_d* and σ_r*.

$$\sigma^* = \gamma G^* \qquad \ldots(33)$$

where γ is the commanded strain and G* is complex modulus at the beginning of the test. Plot of complex modulus vs. time for H5690S is shown in Figure 3.29. In this case, σ_d* and σ_r* were equal to 20 and 10 rad/s, respectively.

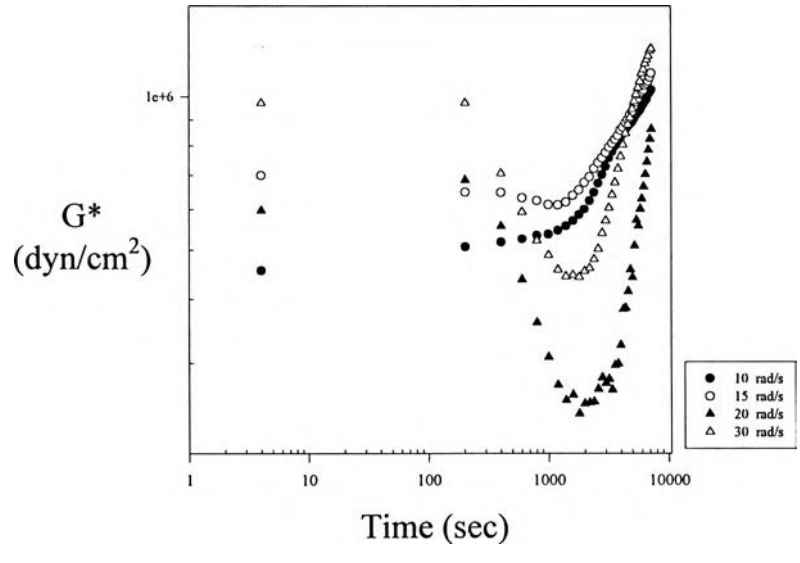

Figure 3.29 Plot of G* vs. time for H5690S sheared at an amplitude of 30% at 200°C.

Overall critical condition is illustrated in Figure 3.30. There are 3 regimes; (I) the regime below σ_r*, in which G* rises more than a factor of 2 within 2 hours, (II) the regime between σ_r* and σ_d*, in which G* rises slightly and then decays but not more than a factor of 2 within 2 hours, and (III) the regime above σ_d*, in which G* decays more than a factor of 2 within 2 hours.

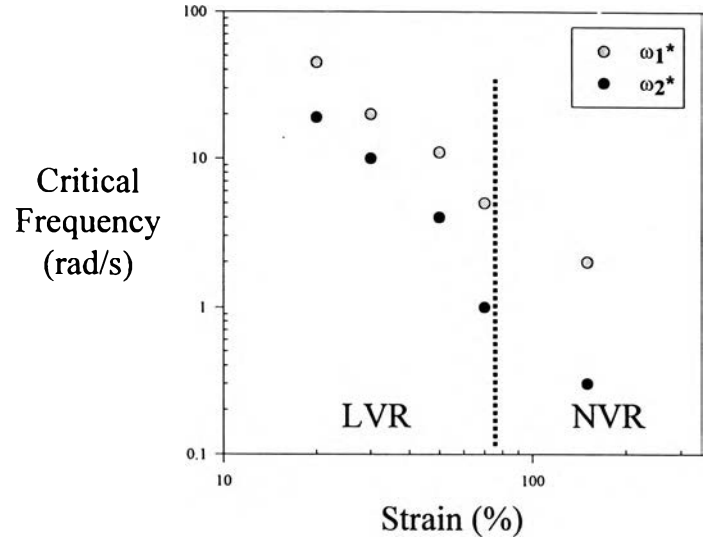

(a)

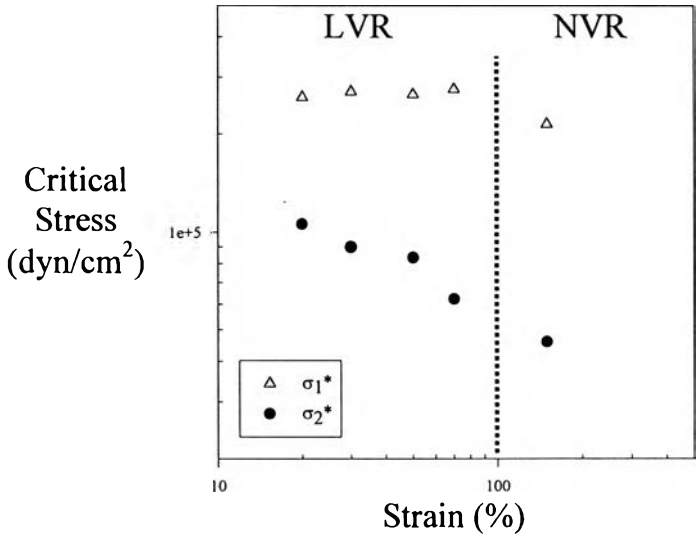

(b)

Figure 3.30 Plot of (a) critical frequency and (b) critical stress vs. strain for H5690S sheared at an amplitude of 30% at 200°C.

3.6.1 Decays in Complex Modulus

The surfaces of sheared H5690S samples after having been sheared at 200°C were studied microscopically by SEM (magnification = 2,000).

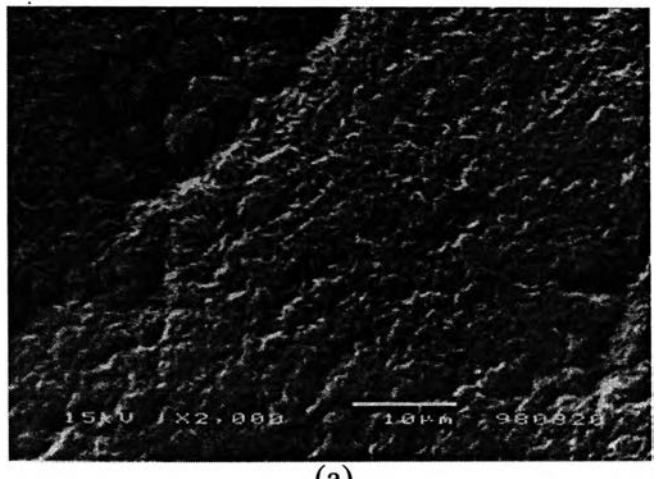

(a)

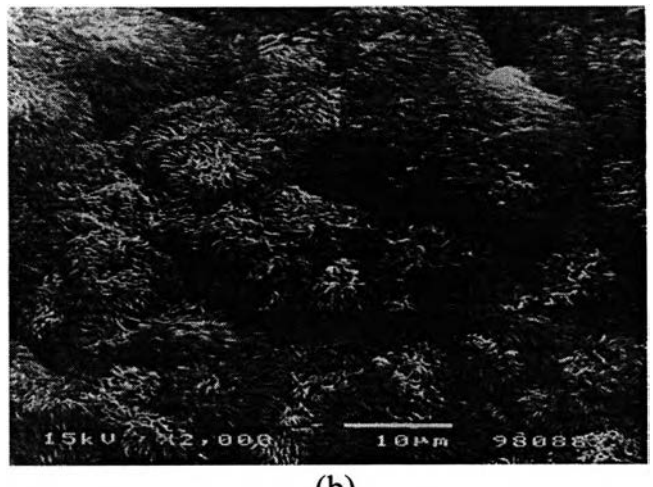

(b)

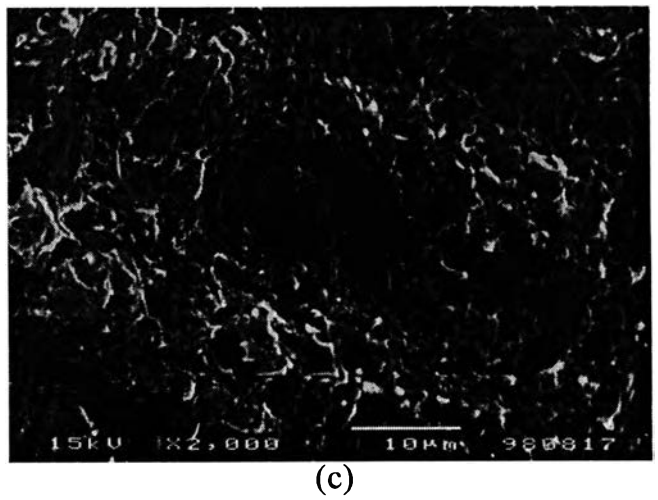

(c)

Figure 3.31 SEM micrographs of H5690S after having been sheared at (a) below ω_d*, (b) ω_d*, and (c) above ω_d* at 200°C.

Below critical condition for G^* decay, no voids were observed on the sample surface. But at the critical condition, voids were observed on the surface texture and seems to increase with increasing frequency. This means voids formation is one of the slip mechanisms at 200°C.

3.6.2 Rises in Complex Modulus

High density polyethylenes are readily crosslinked thermally in the melt in the presence of traces of oxygen (Encyclopedia of Polymer Science & Engineering, Vol.4). Rouse-Mooney theory predicts that if cross-linking forms, the plateau of G^* at low frequency must occur.

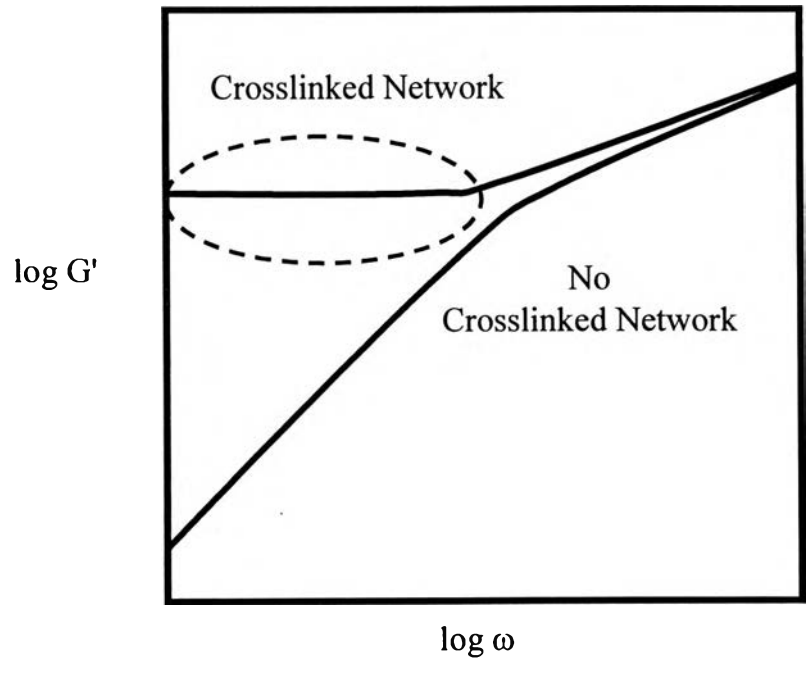

Figure 3.32 Rouse-Mooney theory.

ต้นฉบับ หน้าขาดหาย